

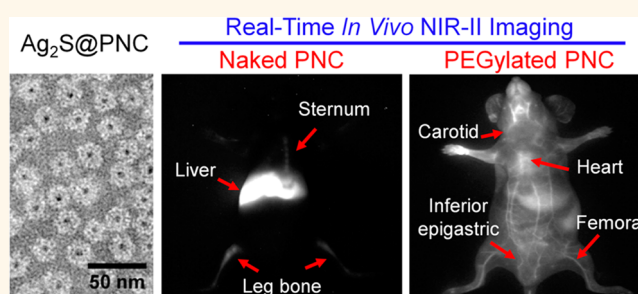
# Real-Time Monitoring Surface Chemistry-Dependent *In Vivo* Behaviors of Protein Nanocages via Encapsulating an NIR-II Ag<sub>2</sub>S Quantum Dot

Chunyan Li,<sup>†</sup> Feng Li,<sup>\*,‡</sup> Yejun Zhang,<sup>†</sup> Wenjing Zhang,<sup>‡</sup> Xian-En Zhang,<sup>§</sup> and Qiangbin Wang<sup>\*,†</sup>

<sup>†</sup>Key Laboratory of Nano-Bio Interface, Division of Nanobiomedicine and *i*-Lab, CAS Center for Excellence in Brain Science, Suzhou Institute of Nano-Tech and Nano-Bionics, Chinese Academy of Sciences, Suzhou 215123, China, <sup>‡</sup>State Key Laboratory of Virology, Wuhan Institute of Virology, Chinese Academy of Sciences, Wuhan 430071, China, and <sup>§</sup>National Laboratory of Biomacromolecules, Institute of Biophysics, Chinese Academy of Sciences, Beijing 100101, China

**ABSTRACT** Protein nanocages (PNCs) have been recognized as a promising platform for nanomedicine innovation. Real-time *in vivo* tracking of PNCs can provide critically important information for the development of PNC-based diagnostics and therapeutics. Here we demonstrate a general strategy for monitoring the behaviors of PNCs *in vivo* by encapsulating a Ag<sub>2</sub>S quantum dot (QD) with fluorescence in the second near-infrared window (NIR-II, 1000–1700 nm) inside the PNC, using simian virus 40 (SV40) PNC (PNC<sub>SV40</sub>) as a model. Benefiting from the high spatiotemporal resolution and deep tissue

penetration of NIR-II fluorescence imaging, the dynamic distribution of the PNC<sub>SV40</sub> in living mice was tracked in real time with high fidelity, and adopting the PEGylation strategy, surface chemistry-dependent *in vivo* behaviors of PNC<sub>SV40</sub> were clearly revealed. This study represents the first evidence of real-time tracking of the intrinsic behaviors of PNCs *in vivo* without interference in PNC-host interactions by encapsulating nanoprobes inside. The as-described imaging strategy will facilitate the study of interactions between exogenously introduced PNCs and host body and prompt the development of future protein-based drugs, sensors, and high-efficacy targeted delivery systems.



**KEYWORDS:** protein nanocage · surface chemistry · *in vivo* imaging · Ag<sub>2</sub>S quantum dots · near-infrared fluorescence

Protein nanocages (PNCs) are a representative group of protein nanostructures generally 10–100 nm in diameter, assembled from multiple copies of subunits.<sup>1</sup> Due to their unique features such as good biocompatibility and direct genetic fusion with peptide/protein drugs, PNCs have been recognized as natural biomedical materials for developing vaccines,<sup>2–4</sup> therapeutic molecules delivery vectors,<sup>5–9</sup> and *in vivo* diagnostic devices.<sup>10–15</sup> The realization of the functions of PNCs *in vivo* is dependent on their transportation, biodistribution, and the protein–host interactions. Real-time *in vivo* tracking of PNCs with high fidelity would offer great convenience to analyzing the *in vivo* behaviors of PNCs and thus to improving the *in vivo*

targeting and functionality of PNCs, substantially benefiting the translation of PNC-based biomedical techniques to practical applications.<sup>16,17</sup>

Despite of the available computed tomography (CT), magnetic resonance imaging (MRI), and nuclear imaging (positron emission tomography [PET] and single photon emission computed tomography [SPECT]), fluorescence probes have been widely used for biomolecular labeling due to their inherent advantages of high sensitivity, fast feedback, multiplexing, and absence of ionizing radiation.<sup>18</sup> However, they are suffering from the limited tissue penetration depth of their classic fluorescence (<900 nm) in *in vivo* imaging.<sup>19</sup> Alternatively, fluorescence imaging in the second near-infrared window

\* Address correspondence to qbwang2008@sinano.ac.cn, fli@wh.iov.cn.

Received for review September 1, 2015 and accepted October 23, 2015.

Published online October 23, 2015  
10.1021/acs.nano.5b05503

© 2015 American Chemical Society

(NIR-II, 1000–1700 nm) provides unprecedented penetration depth and spatiotemporal resolution in comparison with the conventional fluorescence imaging.<sup>20–23</sup> Here, by using a PNC assembled from the major capsid protein of simian virus 40 (SV40), VP1, as a model, and through encapsulating an NIR-II emitting Ag<sub>2</sub>S quantum dot (QD,  $\lambda_{\text{Em}} = 1200$  nm) in the cavity of SV40, we accomplished dynamically tracking the migration and biodistribution of SV40 PNC (PNC<sub>SV40</sub>) *in vivo*.

SV40, a member of polyomaviridae, is one of the simplest double-stranded DNA viruses.<sup>24</sup> SV40 VP1 can form a PNC, which can efficiently encapsulate QD in the cavity through controllable self-assembly while preserving its natural biological activity.<sup>25–27</sup> Due to the intrinsic biological transparency window of tissue, Ag<sub>2</sub>S QD with excellent NIR-II fluorescence enables the *in vivo* imaging with deep tissue penetration (>1.1 cm) and high spatiotemporal resolution of 25  $\mu\text{m}$  and 50 ms, respectively.<sup>28,29</sup> For the first time, the migration dynamics and biodistribution of PNC<sub>SV40</sub> *in vivo* were tracked in real time. It was found that PNC<sub>SV40</sub> was cleared out from the blood circulation within 5 min post intravenous injection (pi) and that PNC<sub>SV40</sub> was mainly accumulated in the reticulo-endothelial system (RES). In contrast, when the surface property of PNC<sub>SV40</sub> was modified through the traditional PEGylation strategy, PEGylated PNC<sub>SV40</sub> behaved dramatically different from the naked PNC<sub>SV40</sub>, showing significantly prolonged blood circulation and much less uptake in the RES. These findings of *in vivo* NIR-II imaging were corroborated by *ex vivo* imaging, inductively coupled plasma mass spectrometry (ICP-MS) analysis, and macrophage endocytosis assay. The *in vivo* PNC tracking strategy described here, with high spatiotemporal resolution and fidelity, provides a visible and direct way to investigate interactions between exogenously introduced PNCs and host body, potentially speeding discovery and innovation in PNC-based nanomedicines.

## RESULTS AND DISCUSSION

Ag<sub>2</sub>S QDs were efficiently encapsulated into PNC<sub>SV40</sub> through a controllable coassembly process of SV40 VP1 and Ag<sub>2</sub>S QDs (see the Methods section for details).<sup>26</sup> Transmission electron microscopy (TEM) revealed that each PNC<sub>SV40</sub> contained one Ag<sub>2</sub>S QD and possessed an average overall diameter of  $24 \pm 1.76$  nm (Figure 1a), which was similar to the native T = 1 virus-like particle of SV40 (Figure S1).<sup>30</sup> The optical properties of the as-prepared Ag<sub>2</sub>S@PNC<sub>SV40</sub> were characterized as shown in Figure 1b. In comparison with free Ag<sub>2</sub>S QDs, the encapsulated Ag<sub>2</sub>S@PNC<sub>SV40</sub> exhibited similar absorbance and fluorescence spectra, except a small red-shifted emission peak probably due to the changed dielectric constant surrounding Ag<sub>2</sub>S QDs.

In order to track SV40 *in vivo* through Ag<sub>2</sub>S QDs fluorescence, the stability of Ag<sub>2</sub>S@PNC<sub>SV40</sub> in serum over a prolonged period would be critical. After incubating the stock of Ag<sub>2</sub>S@PNC<sub>SV40</sub> with serum at 37 °C over different time scales, negative-staining TEM analysis was carried out in which Ag<sub>2</sub>S@PNC<sub>SV40</sub> was clearly distinguished out of the messy background of serum proteins with well-preserved spherical morphology of PNC<sub>SV40</sub> embedding a Ag<sub>2</sub>S QD core (Figures 1c and S2), suggesting good serum stability of Ag<sub>2</sub>S@PNC<sub>SV40</sub>.

The dynamic migration of Ag<sub>2</sub>S@PNC<sub>SV40</sub> in living mouse was tracked in real time under an InGaAs-based shortwave infrared imaging system (Figure 1d and Movie S1 in Supporting Information). After injecting Ag<sub>2</sub>S@PNC<sub>SV40</sub> into a female athymic nude mouse by tail vein, Ag<sub>2</sub>S@PNC<sub>SV40</sub> were observed to migrate rapidly throughout the whole blood vessels at the very beginning and then were mainly accumulated in liver and spleen within 5 min pi. Interestingly, besides the bright fluorescence observed in RES including liver and spleen, Ag<sub>2</sub>S@PNC<sub>SV40</sub> was also found in bone marrow as displaying high NIR-II fluorescence in leg bone and sternum at 12 h pi (Figure 1d). Further, through principal component analysis (PCA), different tissues and organs in the living mouse were unambiguously distinguished based on the dynamic contrast after computation on the first 150 frames of fluorescence pictures within 15 s pi (Figure 1e). Clearly, Ag<sub>2</sub>S-based NIR-II fluorescence imaging provided an unprecedented method to reveal the dynamic transportation of PNC<sub>SV40</sub> *in vivo* with high spatiotemporal resolution and deep tissue penetration.

More and more evidence indicates that surface properties of nanomaterials play a determinant role in regulating their *in vivo* behaviors.<sup>31–35</sup> Intense endeavors have been devoted to reducing nonspecific clearance and enhancing targeting capability of nanomaterials *in vivo*.<sup>36,37</sup> In particular, PEGylation has been successful in reducing nanomaterials accumulation in RES and prolonging their blood circulation time, resulting in increased chance of accumulation in the region of interest (ROI).<sup>17,38</sup> Therefore, PEGylation of PNC<sub>SV40</sub> on its outer surface was carried out to help the escape from nonspecific RES uptake. Two different molecular weights of PEG (PEG750 and PEG5K) were chosen for better understanding of how the PEG affected the *in vivo* performance of PNC<sub>SV40</sub>. The *in vivo* dynamics and distribution of the PEGylated Ag<sub>2</sub>S@PNC<sub>SV40</sub> were analyzed in real time using the aforementioned NIR-II imaging method.

After PEGylation, the Ag<sub>2</sub>S@PNC<sub>SV40</sub>-PEG preserved intact core/shell structure and exhibited similar size and morphology to that of Ag<sub>2</sub>S@PNC<sub>SV40</sub> under TEM (Figure S3) as the PEG chains could not be negatively stained. Dynamic light scattering (DLS) analysis revealed the increased hydrodynamic diameters (HDs)

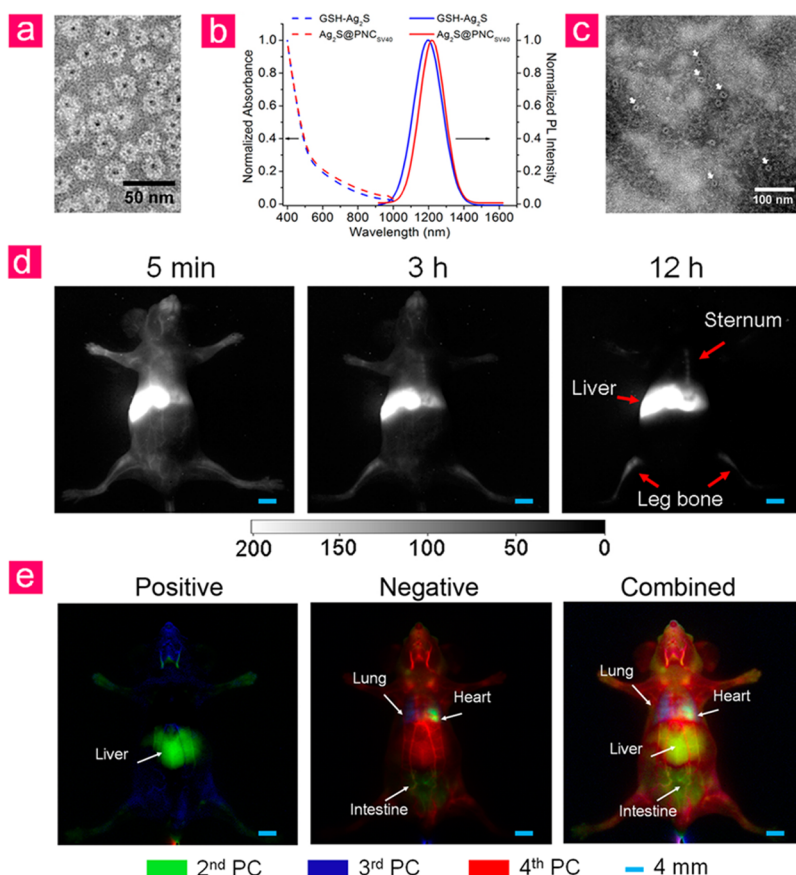


**Figure 1.** Real-time *in vivo* NIR-II fluorescence imaging of PNC<sub>SV40</sub> in virtue of the Ag<sub>2</sub>S QD encapsulated in its cavity. (a) Negative-staining TEM image of Ag<sub>2</sub>S@PNC<sub>SV40</sub>. (b) Absorbance and photoluminescence spectra of Ag<sub>2</sub>S@PNC<sub>SV40</sub> in comparison with glutathion modified Ag<sub>2</sub>S QDs (GSH-Ag<sub>2</sub>S QDs). (c) TEM image of Ag<sub>2</sub>S@PNC<sub>SV40</sub> incubated with serum for 2 days, in which the white arrows indicate typical Ag<sub>2</sub>S@PNC<sub>SV40</sub>. (d) Time course of NIR-II fluorescence images of living mice injected with 200  $\mu$ L (1 mg/mL) Ag<sub>2</sub>S@PNC<sub>SV40</sub>. Images were acquired at 5 min, 3 and 12 h pi, respectively. (e) Dynamic contrast enhanced images with Ag<sub>2</sub>S@PNC<sub>SV40</sub> measured according to VP1 protein content, similarly hereafter, based on PCA analysis, the second (green), third (blue), and fourth (red) principal components (PCs) are retained. PCA images were obtained over the first 15 s (150 frames) pi.

of Ag<sub>2</sub>S@PNC<sub>SV40</sub>-PEG750 and Ag<sub>2</sub>S@PNC<sub>SV40</sub>-PEG5K from  $28.8 \pm 2.34$  nm of Ag<sub>2</sub>S@PNC<sub>SV40</sub> to  $33.2 \pm 1.93$  nm and  $57.1 \pm 2.11$  nm, respectively (Figure 2a), while zeta-potential measurement (Figure 2b) suggests that Ag<sub>2</sub>S@PNC<sub>SV40</sub> and Ag<sub>2</sub>S@PNC<sub>SV40</sub>-PEG750 possessed comparable values around  $-8$  mV, while Ag<sub>2</sub>S@PNC<sub>SV40</sub>-PEG5K was found to be nearly 0 mV (see Table S1). Native gel electrophoresis results indicate that the relative homogeneity of the Ag<sub>2</sub>S@PNC<sub>SV40</sub> and PEGylated Ag<sub>2</sub>S@PNC<sub>SV40</sub>, in which a single band was observed from each sample (Figure 2c). In addition, the Ag<sub>2</sub>S@PNC<sub>SV40</sub> migrated slightly faster than Ag<sub>2</sub>S@PNC<sub>SV40</sub>-PEG750, consistent with the data that Ag<sub>2</sub>S@PNC<sub>SV40</sub> possessed a similar surface charge but smaller HD in comparison to Ag<sub>2</sub>S@PNC<sub>SV40</sub>-PEG750. As for Ag<sub>2</sub>S@PNC<sub>SV40</sub>-PEG5K, the sample was totally trapped in the loading well because of its nearly zero surface charge and a much larger size. These observations confirm that the successful PEGylation of Ag<sub>2</sub>S@PNC<sub>SV40</sub>. Further, matrix-assisted laser desorption ionization-time-of-flight mass spectrometry (MALDI-TOF MS) was utilized to quantify the number of PEG molecules conjugated on

Ag<sub>2</sub>S@PNC<sub>SV40</sub>. Figure 2d shows the MS spectra of the three kinds of PNC<sub>SV40</sub>. The conjugation density of PEG was estimated (see Figure S4 for detailed analysis). It was found that, for Ag<sub>2</sub>S@PNC<sub>SV40</sub>-PEG750, each VP1 was conjugated on average with 12 copies of PEG750 molecules. In contrast, one, two, three, and four PEG5K molecules per VP1 were detected in the Ag<sub>2</sub>S@PNC<sub>SV40</sub>-PEG5K sample.

Intact protein structures (Figure S3), excellent NIR-II fluorescence (Figure S5) and good serum stability (Figure S6) of PEGylated Ag<sub>2</sub>S@PNC<sub>SV40</sub> enabled *in vivo* tracking of the dynamic migration and bio-distribution of PNC<sub>SV40</sub> after PEGylation. As shown in Figure 3a and Movies S2 and S3, both Ag<sub>2</sub>S@PNC<sub>SV40</sub>-PEG750 and Ag<sub>2</sub>S@PNC<sub>SV40</sub>-PEG5K were migrated to the heart and lung at the beginning after intravenous injection and then were pumped into the whole body through the systemic circulation. Unlike the naked Ag<sub>2</sub>S@PNC<sub>SV40</sub> which was rapidly eliminated from bloodstream within 5 min pi, the PEGylated PNC<sub>SV40</sub> exhibited greatly increased blood retention with distinguishable fluorescence signals lasting over 12 h. In particular, for the Ag<sub>2</sub>S@PNC<sub>SV40</sub>-PEG5K, there was

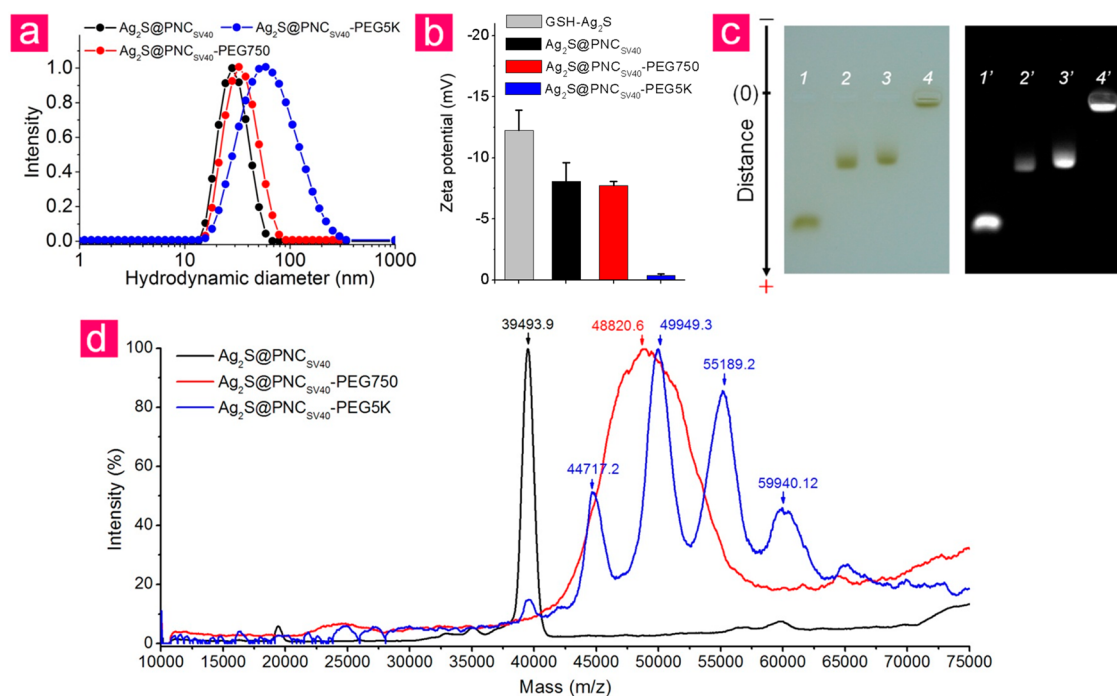


**Figure 2.** Characterization of PEGylated  $\text{Ag}_2\text{S}@PNC_{SV40}$ . (a) HD measurement by DLS. (b) Zeta potential measurement. Results are presented as mean  $\pm$  SD ( $n = 3$ ). (c) Agarose gel electrophoresis. A bright-field color photo (left) and an NIR-II fluorescence image (right) of the agarose gel were recorded. Lanes 1–4 (1'–4'), GSH- $\text{Ag}_2\text{S}$  QDs,  $\text{Ag}_2\text{S}@PNC_{SV40}$ ,  $\text{Ag}_2\text{S}@PNC_{SV40}$ -PEG750, and  $\text{Ag}_2\text{S}@PNC_{SV40}$ -PEG5K, respectively. (d) MALDI-TOF MS analysis for semiquantification of PEGylation efficiency of  $PNC_{SV40}$ .

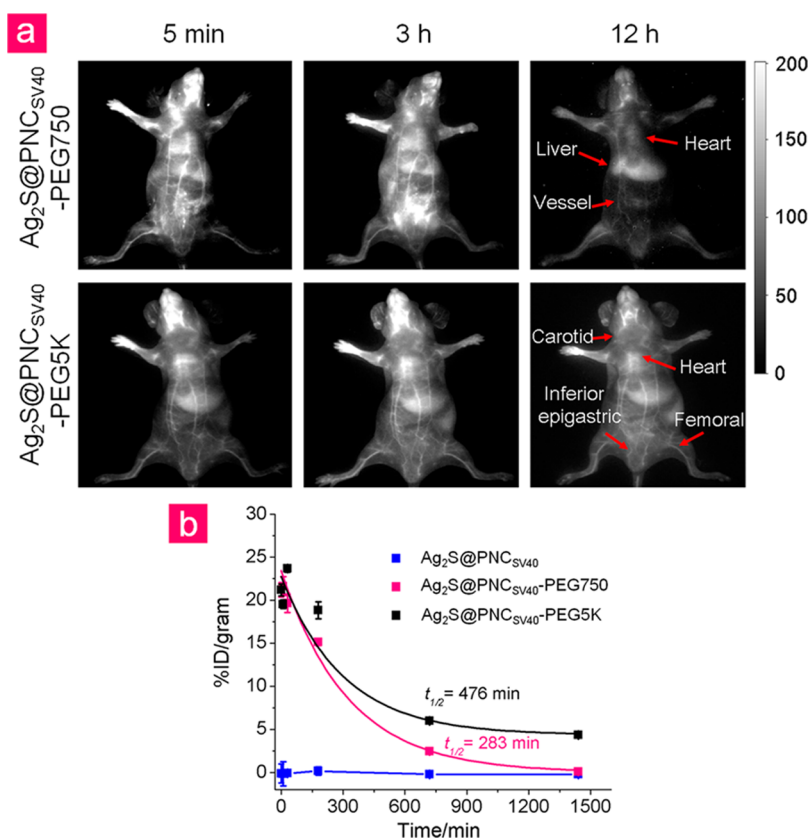


**Figure 3.** (a) Time course of NIR-II fluorescence images of living mice injected with 200  $\mu\text{L}$  (1 mg/mL) of PEGylated  $\text{Ag}_2\text{S}@PNC_{SV40}$ . Images were acquired at 5 min, 3 and 12 h pi, respectively. (b) Blood circulation curves of naked and PEGylated  $\text{Ag}_2\text{S}@PNC_{SV40}$  in mice. Blood samples (20  $\mu\text{L}$ ) were collected at a series of time points pi, and the half-lives of different  $\text{Ag}_2\text{S}@PNC_{SV40}$  in the bloodstream were calculated based on ICP-MS analysis.



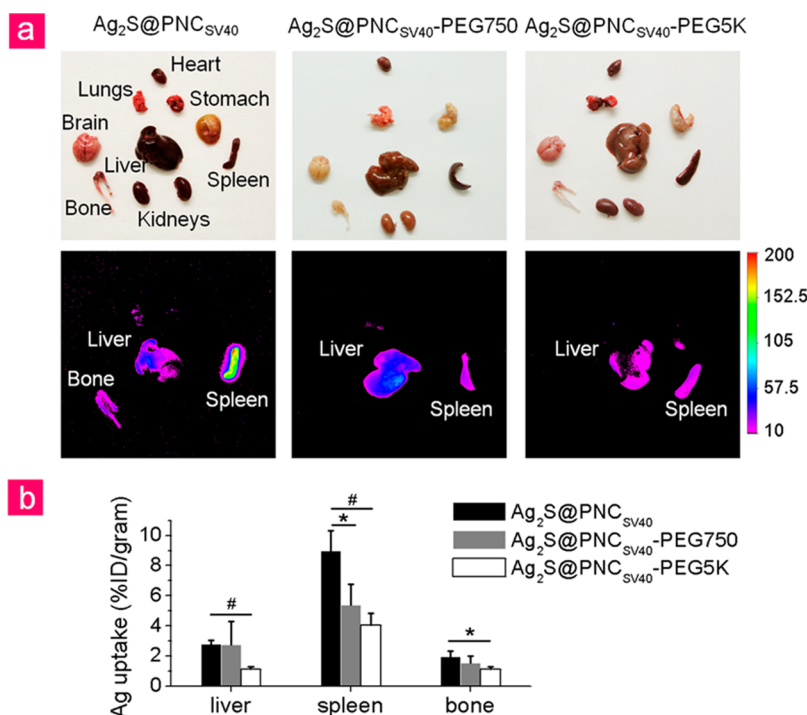


**Figure 4.** *Ex vivo* analysis of the biodistribution of  $\text{Ag}_2\text{S}@PNC_{SV40}$  and PEGylated  $\text{Ag}_2\text{S}@PNC_{SV40}$ . (a) *Ex vivo* bright-field color photos and NIR-II fluorescence images of various tissues and organs taken from the mice injected with  $\text{Ag}_2\text{S}@PNC_{SV40}$ ,  $\text{Ag}_2\text{S}@PNC_{SV40}\text{-PEG750}$ , and  $\text{Ag}_2\text{S}@PNC_{SV40}\text{-PEG5K}$  at 12 h pi. (b) Quantitative analysis of short-term retention of various  $PNC_{SV40}$  in liver, spleen, and bone marrow measured by ICP-MS at 12 h pi. Results are presented as mean  $\pm$  SD ( $n = 3$ ). \* $p < 0.05$ , # $p < 0.01$ .

negligible  $\text{Ag}_2\text{S}$  fluorescence observed in the RES system and bone marrow.

To quantitatively assess the retention of the PEGylated  $\text{Ag}_2\text{S}@PNC_{SV40}$  in bloodstream, the blood circulation half-lives of  $\text{Ag}_2\text{S}@PNC_{SV40}$ ,  $\text{Ag}_2\text{S}@PNC_{SV40}\text{-PEG750}$ , and  $\text{Ag}_2\text{S}@PNC_{SV40}\text{-PEG5K}$  were analyzed by ICP-MS, respectively. As shown in Figure 3b, blood clearance rates of naked  $\text{Ag}_2\text{S}@PNC_{SV40}$  and PEGylated  $\text{Ag}_2\text{S}@PNC_{SV40}$  were quite different. The concentration of  $\text{Ag}_2\text{S}@PNC_{SV40}$  in bloodstream was dramatically decreased to an undetectable level within 5 min pi, which can be explained as that exogenous protein molecules were rapidly opsonized and then cleared by RES upon entry into the bloodstream. In contrast,  $\text{Ag}_2\text{S}@PNC_{SV40}\text{-PEG750}$  and  $\text{Ag}_2\text{S}@PNC_{SV40}\text{-PEG5K}$  exhibited significantly prolonged half-lives of 283 and 476 min in bloodstream, respectively. The half-lives quantified by ICP-MS agreed well with the different fluorescence patterns of naked and PEGylated  $\text{Ag}_2\text{S}@PNC_{SV40}$  in living mice (Figure 3a), supporting the validity of the information delivered by NIR-II imaging.

*In vivo* real-time NIR-II fluorescence imaging clearly reveals that dynamic migration and biodistribution of PEGylated  $\text{Ag}_2\text{S}@PNC_{SV40}$ , and it was observed that PEGylation significantly inhibits the uptake of  $PNC_{SV40}$  by liver, spleen, and bone marrow. To quantitatively check the distribution patterns of the naked  $\text{Ag}_2\text{S}@PNC_{SV40}$  and PEGylated  $\text{Ag}_2\text{S}@PNC_{SV40}$  *in vivo*, *ex vivo* fluorescence quantification and ICP-MS analysis

of  $\text{Ag}_2\text{S}$  content were conducted. As shown in Figure 4a, most of  $\text{Ag}_2\text{S}@PNC_{SV40}$  and PEGylated  $\text{Ag}_2\text{S}@PNC_{SV40}$  were nonspecifically accumulated in spleen and liver. It is notable that the fluorescence intensity in liver, spleen, and bone marrow in the mouse injected with  $\text{Ag}_2\text{S}@PNC_{SV40}$  was much higher than that in the case of PEGylated  $\text{Ag}_2\text{S}@PNC_{SV40}$ . ICP-MS analysis (Figures 4b and S7) showed that the highest uptake of  $\text{Ag}_2\text{S}@PNC_{SV40}$  was in the spleen (8.98%), followed by the liver (2.77%) and bone marrow (1.96%) at 12 h pi. In contrast, PEGylation significantly reduced the internalization of the  $\text{Ag}_2\text{S}@PNC_{SV40}$  in these organs (for  $\text{Ag}_2\text{S}@PNC_{SV40}\text{-PEG750}$ , spleen: 5.39%, liver: 2.74%, and bone marrow: 1.53%; for  $\text{Ag}_2\text{S}@PNC_{SV40}\text{-PEG5K}$ , spleen: 4.05%, liver: 1.11%, and bone marrow: 1.10%). The ICP-MS data are consistent to the fluorescence imaging data, suggesting the high fidelity of  $\text{Ag}_2\text{S}$  NIR-II imaging in monitoring the transportation and distribution of  $PNC_{SV40}$  *in vivo*. Additionally, although  $\text{Ag}_2\text{S}@PNC_{SV40}$  were modified by PEG750 with higher density than by PEG5K, the latter offered better shielding effect against internalization of  $\text{Ag}_2\text{S}@PNC_{SV40}$  in RES including spleen, liver, and bone marrow. Similar effects were observed for other macromolecules, which is ascribed to that PEG molecules of larger molecular weights are thought to provide thicker shielding layers.<sup>39</sup> Taken together, these results have demonstrated that PEGylation changed the spatiotemporal distribution of  $PNC_{SV40}$  *in vivo* and greatly reduced the nonspecific uptake of  $\text{Ag}_2\text{S}@PNC_{SV40}$  by

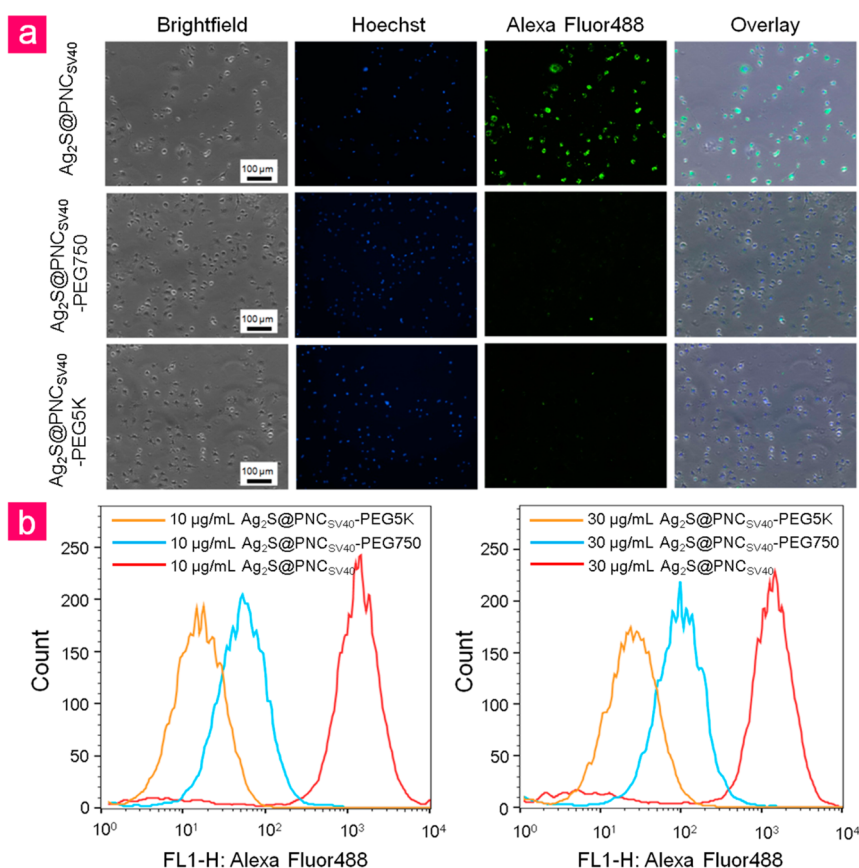


**Figure 5.** Comparison of interactions between macrophages and Ag<sub>2</sub>S@PNC<sub>SV40</sub> of different surface properties. (a) Fluorescence microscope images of living RAW 264.7 cells incubated with 20 µg/mL Alexa Fluor488 conjugated Ag<sub>2</sub>S@PNC<sub>SV40</sub>, Ag<sub>2</sub>S@PNC<sub>SV40</sub>-PEG750, or Ag<sub>2</sub>S@PNC<sub>SV40</sub>-PEG5K and then further with Hoechst 33258. (b) Flow cytometric histogram profiles of different PNC<sub>SV40</sub> in RAW 264.7 cells after incubation for 3 h.

liver, spleen, and bone marrow, which will have great potential in improving the passive targeting efficacy of the PNCs as delivery vectors. More importantly, these observations have manifested that NIR-II imaging is a direct and reliable way to real-time track the distribution of PNCs *in vivo* and is a facile technique to precisely evaluate the surface property-dependent behaviors of PNCs *in vivo*.

To understand the observed *in vivo* shielding effect of PEGylation on Ag<sub>2</sub>S@PNC<sub>SV40</sub>, the interactions of Ag<sub>2</sub>S@PNC<sub>SV40</sub>, Ag<sub>2</sub>S@PNC<sub>SV40</sub>-PEG750, and Ag<sub>2</sub>S@PNC<sub>SV40</sub>-PEG5K with macrophages were carefully studied. Macrophage, as a representative cell type in the RES, *e.g.*, liver and spleen, plays a central role in protecting the body from foreign substances and microbes in innate immunity. How the Ag<sub>2</sub>S@PNC<sub>SV40</sub> interacts with macrophages will provide insights in understanding their *in vivo* behaviors. Therefore, endocytosis assay of various Ag<sub>2</sub>S@PNC<sub>SV40</sub> by activated mouse-derived macrophages, RAW264.7, was carried out. For *in vitro* fluorescence microscope and fluorescence-activated cell sorting (FACS) assay, Alexa Fluor488 dye was conjugated onto the cysteines of VP1, and it was confirmed that all the Ag<sub>2</sub>S@PNC<sub>SV40</sub> formulations at the same concentration of PNC<sub>SV40</sub>

gave equivalent fluorescence intensity of Alexa Fluor488 (Figure S8). After incubation with various Ag<sub>2</sub>S@PNC<sub>SV40</sub> conjugated with Alexa Fluor488 dye in phosphate buffered saline (PBS), RAW264.7 cells incubated with Ag<sub>2</sub>S@PNC<sub>SV40</sub> displayed intense fluorescence of Alexa Fluor488, whereas there was much less fluorescence in the cells incubated with PEGylated Ag<sub>2</sub>S@PNC<sub>SV40</sub> under the same condition (Figure 5a), suggesting that PEGylation greatly suppressed the internalization of the PNC<sub>SV40</sub> by macrophages. As detected by FACS (Figure 5b), by plotting the phagocytosis efficiency versus Ag<sub>2</sub>S@PNC<sub>SV40</sub> with different surface properties, similar results to the cell imaging were obtained. Quantitative analysis of fluorescence intensity in the Ag<sub>2</sub>S@PNC<sub>SV40</sub> group showed nearly 100-fold higher than that in the Ag<sub>2</sub>S@PNC<sub>SV40</sub>-PEG5K group under the same incubation condition. And there was much less Ag<sub>2</sub>S@PNC<sub>SV40</sub> uptake by RAW264.7 cells for PEGylation with PEG5K than with PEG750, indicating enhanced shielding effect with increased PEG molecular weight. These data are consistent with the significantly prolonged *in vivo* blood circulation time of PEGylated Ag<sub>2</sub>S@PNC<sub>SV40</sub> and also suggest that modifying PNCs with PEG of larger molecular weights is more suitable for *in vivo* biomedical applications that

need immuno shielding. Taken together, the cellular uptake assays provide an explanation for the *in vivo* shielding effect of PEGylation on Ag<sub>2</sub>S@PNC<sub>SV40</sub> and also additionally verify the information revealed by NIR-II imaging.

## CONCLUSION

In summary, we have achieved the real-time tracking of *in vivo* immigration dynamics and distribution of PNCs in virtue of NIR-II fluorescence imaging by encasing an Ag<sub>2</sub>S QD inside. In principle, such a QD-encapsulating strategy for labeling PNCs does not interfere with the molecular or cellular interactions between PNCs and the host body, in comparison with linking QDs to the external surface of PNCs, as well as avoid exposure to the nuclear radiation in the case of nuclear medicine detection methods of CT, PET, SPECT, etc. The advantageous NIR-II fluorescence property of Ag<sub>2</sub>S QDs enabled the tracking of PNC<sub>SV40</sub> in living mice for a long period of time with high stability, fidelity, and spatiotemporal resolution. As clearly revealed by the NIR-II fluorescence imaging, PNC<sub>SV40</sub>

were rapidly cleared from the bloodstream and selectively accumulated mainly in liver, spleen, and bone marrow, but surface PEGylation of PNC<sub>SV40</sub> significantly prolonged its blood circulation time from <5 to 476 min and resulted in quite different *in vivo* behaviors of PNC<sub>SV40</sub>, the molecular mechanism underlying which should be investigated in terms of receptor recognition, biomolecule corona formation, and so on in future for better regulation of PNC–host interactions. These findings successfully demonstrated the importance of the surface property of the PNCs on their *in vivo* behaviors and the feasibility of Ag<sub>2</sub>S QD in real-time tracking of PNCs *in vivo* for its NIR-II fluorescence with deeper penetration depth and higher spatiotemporal resolution. The Ag<sub>2</sub>S QD-encapsulated strategy can be generalized to other caged protein materials and promises new insights into interactions between exogenously introduced caged protein materials and host body, which is essential for rational design and optimization of surface properties for PNC-based *in vivo* biomedical applications, like vaccine, biosensing, and targeted delivery.

## METHODS

**Materials.** Unless otherwise noted, all chemicals were obtained from commercial sources and used without further purification. 1-Dodecanethiol (DT, 98%), AgNO<sub>3</sub>, (C<sub>2</sub>H<sub>5</sub>)<sub>2</sub>NCS<sub>2</sub>Na·3H<sub>2</sub>O (NaDDTC), and glutathione (GSH) were purchased from Sinopharm Chemical Reagent Co., Ltd. (China). Water with a resistivity value of 18 MΩ·cm<sup>−1</sup> was obtained from a Milli-Q ion-exchange system (Millipore, USA). Amicon Ultra-15 Centrifugal Filter Units with 100 kDa MW cutoff were purchased from Millipore (USA). Alexa Fluor 488 C<sub>5</sub>-maleimide, methoxy PEG750 succinimidyl succinamide, and methoxy PEG5K succinimidyl succinamide were purchased from Thermo Fisher Scientific Inc. (USA), Sigma-Aldrich Co. LLC (USA), and JenKem Technology Co., Ltd. (China), respectively.

**Synthesis of GSH-Ag<sub>2</sub>S QDs.** First, hydrophobic Ag<sub>2</sub>S QDs were synthesized according to previous reports.<sup>40,41</sup> In a typical synthetic process, a mixture of 0.1 mmol of (C<sub>2</sub>H<sub>5</sub>)<sub>2</sub>NCS<sub>2</sub>Ag and 10 g of DT was added into a three-necked flask. After oxygen was removed from the flask, the solution was heated to 210 °C and kept at this temperature for 1 h under N<sub>2</sub> atmosphere. When the mixture was cooled to room temperature (RT), excess of ethanol was added, and then the precipitates were collected through centrifugation. DT-Ag<sub>2</sub>S QDs about 5.6 nm in diameter were obtained. To make Ag<sub>2</sub>S QDs hydrophilic, GSH as a surface ligand was introduced to displace DT, and then GSH-Ag<sub>2</sub>S QDs were obtained.

**Assembly of Ag<sub>2</sub>S@PNC<sub>SV40</sub>.** VP1 was expressed in *E. coli* and purified as described previously.<sup>25</sup> VP1 pentamers (ca. 0.5 mg/mL) in the dissociation buffer (10 mM Tris-HCl pH 8.8, 200 mM NaCl, 2 mM EDTA, 2 mM dithiothreitol, and 5% glycerol) and GSH-Ag<sub>2</sub>S QDs (1.5 mg/mL) were mixed at a molar ratio of 12:1 and exhaustively dialyzed against the encapsulation buffer (10 mM Tris-HCl pH 7.2, 1 mM CaCl<sub>2</sub>, 250 mM NaCl, and 5% glycerol) at 4 °C. The assembly product was concentrated to a VP1 concentration of ca. 4 mg/mL using an Amicon Ultra-15 Centrifugal Filter Unit with 100 kDa MW cutoff (Millipore), then loaded onto a 10%–50% sucrose gradient and centrifuged at 38,000 rpm at 4 °C for 4.5 h in a SW40 rotor (Beckman). Afterward, the brown sharp band in the middle of tube was harvested, followed by exhaustive dialysis against 10 mM PBS, and concentrated to a VP1 concentration of ca. 5 mg/mL using the 100 kDa cutoff filter unit.

**Conjugation of Ag<sub>2</sub>S@PNC<sub>SV40</sub>.** For PEGylation, Ag<sub>2</sub>S@PNC<sub>SV40</sub> (ca. 5 mg/mL, measured according to VP1 protein) stock was directly mixed with preweighted methoxy PEG750 succinimidyl succinamide or methoxy PEG5K succinimidyl succinamide at molar ratios of VP1 monomer:PEG = 1:1117 and 1:280, respectively, incubated first at RT for 40 min and then at 4 °C overnight. Free PEG was removed by dialysis against 10 mM PBS at 4 °C using 50,000 MW cutoff dialysis membrane. For labeling with Alexa Fluor 488, naked or PEGylated Ag<sub>2</sub>S@PNC<sub>SV40</sub> was mixed with Alexa Fluor 488 C<sub>5</sub>-maleimide at a 1:10 molar ratio of VP1 monomer to dye and incubated at 4 °C overnight. Free Alexa Fluor 488 dyes were eliminated by dialysis. The Alexa Fluor 488 labeling efficiency was examined using UV–vis absorption spectrometry and fluorescence spectrometry.

**Characterizations.** *Transmission Electron Microscopy (TEM).* All samples were negatively stained using a previous procedure<sup>3</sup> and observed by an FEI Tecnai 20 TEM equipped with a Gatan UltraScan 894 CCD camera or a Hitachi H7000 TEM equipped with an Olympus MegaView G2 camera. For serum stability analysis, naked or PEGylated Ag<sub>2</sub>S@PNC<sub>SV40</sub> and mouse serum were mixed well with the final concentration of PNC<sub>SV40</sub> as 0.5 mg/mL and that of serum as 50%. To suppress microorganism growth, penicillin-streptomycin was added at a 2× final concentration. The mixtures were incubated at 37 °C and then examined with TEM after 2, 4, and 7 days, respectively.

*UV–vis-NIR Absorption and Fluorescence Spectroscopy.* The UV–vis-NIR absorption spectra of GSH-Ag<sub>2</sub>S QDs and various Ag<sub>2</sub>S@PNC<sub>SV40</sub> were measured by a PerkinElmer Lambda 25 UV–vis spectrometer. The NIR fluorescence spectrum of Ag<sub>2</sub>S QDs was measured using an Applied NanoFluorescence spectrometer (USA) with an excitation laser source of 658 nm. And the fluorescence spectrum of Alexa Fluor 488 was measured on a PerkinElmer LS 55 luminescence spectrometer using an excitation wavelength of 480 nm.

*Dynamic Light Scattering (DLS) and Zeta Potential Measurement.* Samples were loaded in 2 mL cuvettes and run at 10% power (to prevent saturated counts), and hydrodynamic diameters of various Ag<sub>2</sub>S@PNC<sub>SV40</sub> were measured using a Malvern Nanosizer Nano ZS (UK). Zeta potentials of the PNC<sub>SV40</sub> were measured using the same instrument. Each sample was run 3 times.

**Agarose Gel Electrophoresis.** Solution (10  $\mu$ L) of each sample was mixed with 20% ficoll and then analyzed by 1% agarose gel electrophoresis using a Mini-sub cell GT Gel electrophoresis system (Bio-Rad Laboratories Inc.). Ending the electrophoresis, pictures were taken under the irradiation of white light and 808 nm laser, respectively.

**Matrix-Assisted Laser Desorption Ionization-Time-of-Flight Mass Spectrometry (MALDI-TOF MS).** Samples were dialyzed exhaustively against ultrapure water at 4 °C to get rid of any salt and then added with  $\beta$ -mercaptoethanol at a final concentration of 20 mM to break the inter-VP1 disulfide linkage. After incubation at 37 °C for 40 min, trifluoroacetic acid was added at a final concentration of 0.1%, followed by centrifugation at 13,000 *g* for 10 min to remove aggregated QDs. The resulting supernatant was examined by a 4800 MALDI TOF/TOF instrument (AB SCIEX) with sinapic acid as the matrix. Mass spectra were recorded in the range of *m/z* 9942–400,000. Data were processed using Data Explorer (TM) Software V4.5.

**Cell Culture and Fluorescence Imaging.** The mouse macrophage cell line RAW264.7 was provided by the Institute of Biochemistry and Cell Biology, SIBS, CAS (China). The cells were grown in Dulbecco's modified Eagle's medium (DMEM) supplemented with 10% fetal bovine serum (FBS) at 37 °C under 5% CO<sub>2</sub>. For living cell imaging, RAW264.7 cells ( $5 \times 10^5$ /mL) were plated on 14 mm glass coverslips and allowed to adhere for 12 h. The cells were washed with PBS and then incubated with 20  $\mu$ g/mL Alexa Fluor488 conjugated Ag<sub>2</sub>S@PNC<sub>SV40</sub>, Ag<sub>2</sub>S@PNC<sub>SV40</sub>-PEG750, and Ag<sub>2</sub>S@PNC<sub>SV40</sub>-PEG5K, respectively, in PBS for 3 h at 37 °C, and further incubated with Hoechst 33258 for 20 min before fluorescence microscopy imaging.

**Flow Cytometry Analysis.** Cellular uptake of various Ag<sub>2</sub>S@PNC<sub>SV40</sub> in PBS was assessed by means of flow cytometry (BD FACSCalibur). RAW264.7 cells were incubated with 10 or 30  $\mu$ g/mL Alexa Fluor488 conjugated Ag<sub>2</sub>S@PNC<sub>SV40</sub>, Ag<sub>2</sub>S@PNC<sub>SV40</sub>-PEG750, and Ag<sub>2</sub>S@PNC<sub>SV40</sub>-PEG5K, respectively, for 3 h at 37 °C, then harvested, rinsed in PBS, resuspended, and examined by flow cytometry.

**In Vivo and ex Vivo Fluorescence Imaging of Mice.** NIR-II fluorescence imaging, including *in vivo* whole-body fluorescence imaging and *ex vivo* fluorescence imaging of organs and tissues, was performed with a home-built NIR-II fluorescence imaging system. The excitation light was provided by an 808 nm diode laser and filtered by an 880 nm long-pass filter. The dynamic distribution of the Ag<sub>2</sub>S@PNC<sub>SV40</sub> in living mouse was monitored in real time by a continuous record by using an InGaAs camera under illumination of an 808 nm laser diode at a power density of  $\sim 50$  mW cm<sup>-2</sup> and an exposure time of 100 ms.

**Biodistribution.** The organs, tissues, and excreta of mice injected with different Ag<sub>2</sub>S@PNC<sub>SV40</sub>, including brain, heart, lungs, liver, spleen, kidneys, intestine, bone, urine, and feces were weighted and then dissolved in a digest solution (HNO<sub>3</sub>/HClO<sub>4</sub> v/v = 4/1). The uptake of various Ag<sub>2</sub>S@PNC<sub>SV40</sub> in different tissues and organs was determined by ICP-MS (Thermo E. IRIS Duo) analysis of Ag<sup>+</sup> content.

**Statistical analysis.** All data were expressed as the mean  $\pm$  SD and statistical difference between two groups was determined using an unpaired, two-tailed *t* test. *P* < 0.05 was considered to be statistically significant.

**Conflict of Interest:** The authors declare no competing financial interest.

**Acknowledgment.** This work was financially supported by Chinese Academy of Sciences "Strategic Priority Research Program" (XDA01030200), the Key Research Program of the Chinese Academy of Sciences (KGZD-EW-T02-3), the Ministry of Science and Technology of China (2011CB965004), National Natural Science Foundation of China (21303249, 31271076, 21425103, 31470931, 81401464, and 21501192), and Natural Science Foundation of Jiangsu Province (BK2012007 and BK20130366). We are very grateful to Prof. Dan Luo at Cornell University for critical proofreading of the manuscript.

**Supporting Information Available:** The Supporting Information is available free of charge on the ACS Publications website at DOI: 10.1021/acsnano.5b05503.

Supporting results (PDF)

Movie 1 (MPG)

Movie 2 (MPG)

Movie 3 (MPG)

## REFERENCES AND NOTES

- Molino, N. M.; Wang, S. W. Caged Protein Nanoparticles for Drug Delivery. *Curr. Opin. Biotechnol.* **2014**, *28*, 75–82.
- Kanekiyo, M.; Wei, C. J.; Yassine, H. M.; McTamney, P. M.; Boyington, J. C.; Whittle, J. R. R.; Rao, S. S.; Kong, W. P.; Wang, L. S.; Nabel, G. J. Self-Assembling Influenza Nanoparticle Vaccines Elicit Broadly Neutralizing H1N1 Antibodies. *Nature* **2013**, *499*, 102–106.
- Wei, D. Q.; Zhao, X.; Chen, L. M.; Lan, X. G.; Li, Y. H.; Lin, Y.; Wang, Q. Viral Nanoparticles as Antigen Carriers: Influence of Shape on Humoral Immune Responses. *RSC Adv.* **2014**, *4*, 23017–23021.
- Rynda-Appl, A.; Patterson, D. P.; Douglas, T. Virus-like Particles as Antigenic Nanomaterials for Inducing Protective Immune Responses in the Lung. *Nanomedicine* **2014**, *9*, 1857–1868.
- Liang, M. M.; Fan, K. L.; Zhou, M.; Duan, D. M.; Zheng, J. Y.; Yang, D. L.; Feng, J.; Yan, X. Y. H-Ferritin-Nanocaged Doxorubicin Nanoparticles Specifically Target and Kill Tumors with a Single-Dose Injection. *Proc. Natl. Acad. Sci. U. S. A.* **2014**, *111*, 14900–14905.
- Zhen, Z. P.; Tang, W.; Chen, H. M.; Lin, X.; Todd, T.; Wang, G.; Cowger, T.; Chen, X. Y.; Xie, J. RGD-Modified Apoferritin Nanoparticles for Efficient Drug Delivery to Tumors. *ACS Nano* **2013**, *7*, 4830–4837.
- Yildiz, I.; Lee, K. L.; Chen, K.; Shukla, S.; Steinmetz, N. F. Infusion of Imaging and Therapeutic Molecules into the Plant Virus-Based Carrier Cowpea Mosaic Virus: Cargo-Loading and Delivery. *J. Controlled Release* **2013**, *172*, 568–578.
- Anand, P.; O'Neil, A.; Lin, E.; Douglas, T.; Holford, M. Tailored Delivery of Analgesic Ziconotide across a Blood Brain Barrier Model using Viral Nanocontainers. *Sci. Rep.* **2015**, *5*, 12497.
- Ma, Y. J.; Nolte, R. J. M.; Cornelissen, J. J. L. M. Virus-Based Nanocarriers for Drug Delivery. *Adv. Drug Delivery Rev.* **2012**, *64*, 811–825.
- Sun, C. J.; Yang, H.; Yuan, Y.; Tian, X.; Wang, L. M.; Guo, Y.; Xu, L.; Lei, J. L.; Gao, N.; Anderson, G. J.; et al. Controlling Assembly of Paired Gold Clusters within Apoferritin Nanoreactor for *In Vivo* Kidney Targeting and Biomedical Imaging. *J. Am. Chem. Soc.* **2011**, *133*, 8617–8624.
- Cao, C.; Wang, X.; Cai, Y.; Sun, L.; Tian, L.; Wu, H.; He, X.; Lei, H.; Liu, W.; Chen, G.; Zhu, R.; Pan, Y. Targeted *In Vivo* Imaging of Microscopic Tumors with Ferritin-Based Nanoparticles across Biological Barriers. *Adv. Mater.* **2014**, *26*, 2566–2571.
- Lin, X.; Xie, J.; Zhu, L.; Lee, S.; Niu, G.; Ma, Y.; Kim, K.; Chen, X. Y. Hybrid Ferritin Nanoparticles as Activatable Probes for Tumor Imaging. *Angew. Chem., Int. Ed.* **2011**, *50*, 1569–1572.
- Li, K.; Nguyen, H. G.; Lu, X. B.; Wang, Q. Viruses and Their Potential in Bioimaging and Biosensing Applications. *Analyst* **2010**, *135*, 21–27.
- Leong, H. S.; Steinmetz, N. F.; Abblack, A.; Destito, G.; Zijlstra, A.; Stuhlmann, H.; Manchester, M.; Lewis, J. D. Intravital Imaging of Embryonic and Tumor Neovasculature using Viral Nanoparticles. *Nat. Protoc.* **2010**, *5*, 1406–1417.
- Uchida, M.; Flenniken, M. L.; Allen, M.; Willits, D. A.; Crowley, B. E.; Brumfield, S.; Willis, A. F.; Jackiw, L.; Jutila, M.; Young, M. J.; et al. Targeting of Cancer Cells with Ferrimagnetic Ferritin Cage Nanoparticles. *J. Am. Chem. Soc.* **2006**, *128*, 16626–16633.
- Blow, N. *In Vivo* Molecular Imaging: the Inside Job. *Nat. Methods* **2009**, *6*, 465–469.
- Bruckman, M. A.; Randolph, L. N.; VanMeter, A.; Hern, S.; Shoffstall, A. J.; Taurog, R. E.; Steinmetz, N. F. Biodistribution, Pharmacokinetics, and Blood Compatibility of Native and PEGylated Tobacco Mosaic Virus Nano-Rods and -Spheres in Mice. *Virology* **2014**, *449*, 163–173.



18. Weissleder, R.; Pittet, M. J. Imaging in the Era of Molecular Oncology. *Nature* **2008**, *452*, 580–583.
19. Gao, X. H.; Cui, Y. Y.; Levenson, R. M.; Chung, L. W. K.; Nie, S. M. *In Vivo* Cancer Targeting and Imaging with Semiconductor Quantum Dots. *Nat. Biotechnol.* **2004**, *22*, 969–976.
20. Hong, G. S.; Lee, J. C.; Robinson, J. T.; Raaz, U.; Xie, L. M.; Huang, N. F.; Cooke, J. P.; Dai, H. J. Multifunctional *In Vivo* Vascular Imaging using Near-Infrared II Fluorescence. *Nat. Med.* **2012**, *18*, 1841–1846.
21. Hong, G. S.; Robinson, J. T.; Zhang, Y. J.; Diao, S.; Antaris, A. L.; Wang, Q.; Dai, H. J. *In Vivo* Fluorescence Imaging with Ag<sub>2</sub>S Quantum Dots in the Second Near-Infrared Region. *Angew. Chem., Int. Ed.* **2012**, *51*, 9818–9821.
22. Chen, G.; Tian, F.; Zhang, Y.; Zhang, Y.; Li, C.; Wang, Q. Tracking of Transplanted Human Mesenchymal Stem Cells in Living Mice using Near-Infrared Ag<sub>2</sub>S Quantum Dots. *Adv. Funct. Mater.* **2014**, *24*, 2481–2488.
23. Smith, A. M.; Mancini, M. C.; Nie, S. M. Bioimaging: Second Window for *In Vivo* Imaging. *Nat. Nanotechnol.* **2009**, *4*, 710–711.
24. Liddington, R. C.; Yan, Y.; Moulai, J.; Sahli, R.; Benjamin, T. L.; Harrison, S. C. Structure of Simian Virus 40 at 3.8-Å Resolution. *Nature* **1991**, *354*, 278–284.
25. Li, F.; Li, K.; Cui, Z. Q.; Zhang, Z. P.; Wei, H. P.; Gao, D.; Deng, J. Y.; Zhang, X. E. Viral Coat Proteins as Flexible Nano-Building-Blocks for Nanoparticle Encapsulation. *Small* **2010**, *6*, 2301–2308.
26. Li, F.; Chen, H. L.; Zhang, Y. J.; Chen, Z.; Zhang, Z. P.; Zhang, X. E.; Wang, Q. Three-Dimensional Gold Nanoparticle Clusters with Tunable Cores Templated by a Viral Protein Scaffold. *Small* **2012**, *8*, 3832–3838.
27. Li, F.; Zhang, Z. P.; Peng, J.; Cui, Z. Q.; Pang, D. W.; Li, K.; Wei, H. P.; Zhou, Y. F.; Wen, J. K.; Zhang, X. E. Imaging Viral Behavior in Mammalian Cells with Self-Assembled Capsid-Quantum-Dot Hybrid Particles. *Small* **2009**, *5*, 718–726.
28. Li, C. Y.; Zhang, Y. J.; Wang, M.; Zhang, Y.; Chen, G. C.; Li, L.; Wu, D. M.; Wang, Q. *In Vivo* Real-Time Visualization of Tissue Blood Flow and Angiogenesis using Ag<sub>2</sub>S Quantum Dots in the NIR-II Window. *Biomaterials* **2014**, *35*, 393–400.
29. Li, C.; Cao, L.; Zhang, Y.; Yi, P.; Wang, M.; Tan, B.; Deng, Z.; Wu, D.; Wang, Q. Preoperative Detection and Intraoperative Visualization of Brain Tumors for More Precise Surgery: A New Dual-Modality MRI and NIR Nanoprobe. *Small* **2015**, *11*, 4517–4525.
30. Li, F.; Gao, D.; Zhai, X.; Chen, Y.; Fu, T.; Wu, D.; Zhang, Z. P.; Zhang, X. E.; Wang, Q. Tunable, Discrete, Three-Dimensional Hybrid Nanoarchitectures. *Angew. Chem., Int. Ed.* **2011**, *50*, 4202–4205.
31. Tenzer, S.; Docter, D.; Kuharev, J.; Musyanovych, A.; Fetz, V.; Hecht, R.; Schlenk, F.; Fischer, D.; Kiouptsi, K.; Reinhardt, C.; et al. Rapid Formation of Plasma Protein Corona Critically Affects Nanoparticle Pathophysiology. *Nat. Nanotechnol.* **2013**, *8*, 772–781.
32. Dai, Q.; Walkey, C.; Chan, W. C. Polyethylene Glycol Backfilling Mitigates the Negative Impact of the Protein Corona on Nanoparticle Cell Targeting. *Angew. Chem., Int. Ed.* **2014**, *53*, 5093–5096.
33. Calatayud, M. P.; Sanz, B.; Raffa, V.; Riggio, C.; Ibarra, M. R.; Goya, G. F. The Effect of Surface Charge of Functionalized Fe<sub>3</sub>O<sub>4</sub> Nanoparticles on Protein Adsorption and Cell Uptake. *Biomaterials* **2014**, *35*, 6389–6399.
34. Setyawati, M. I.; Tay, C. Y.; Docter, D.; Stauber, R. H.; Leong, D. T. Understanding and Exploiting Nanoparticles' Intimacy with the Blood Vessel and Blood. *Chem. Soc. Rev.* **2015**, *10.1039/C5CS00499C*.
35. Docter, D.; Westmeier, D.; Markiewicz, M.; Stolte, S.; Knauer, S. K.; Stauber, R. H. The Nanoparticle Biomolecule Corona: Lessons Learned-Challenge Accepted? *Chem. Soc. Rev.* **2015**, *44*, 6094–6121.
36. Gref, R.; Domb, A.; Quellec, P.; Blunk, T.; Muller, R. H.; Verbavatz, J. M.; Langer, R. The Controlled Intravenous Delivery of Drugs using PEG-Coated Sterically Stabilized Nanospheres. *Adv. Drug Delivery Rev.* **1995**, *16*, 215–233.
37. Bertrand, N.; Wu, J.; Xu, X. Y.; Kamaly, N.; Farokhzad, O. C. Cancer Nanotechnology: the Impact of Passive and Active Targeting in the Era of Modern Cancer Biology. *Adv. Drug Delivery Rev.* **2014**, *66*, 2–25.
38. Vannucci, L.; Falvo, E.; Fornara, M.; Di Micco, P.; Benada, O.; Krizan, J.; Svoboda, J.; Hulikova-Capkova, K.; Morea, V.; et al. Selective Targeting of Melanoma by PEG-Masked Protein-Based Multifunctional Nanoparticles. *Int. J. Nanomed.* **2012**, *7*, 1489–1509.
39. Wortmann, A.; Vohringer, S.; Engler, T.; Corjon, S.; Schirmbeck, R.; Reimann, J.; Kochanek, S.; Kreppel, F. Fully Detargeted Polyethylene Glycol-Coated Adenovirus Vectors are Potent Genetic Vaccines and Escape from Pre-Existing Anti-Adenovirus Antibodies. *Mol. Ther.* **2008**, *16*, 154–162.
40. Zhang, Y. J.; Liu, Y. S.; Li, C. Y.; Chen, X. Y.; Wang, Q. Controlled Synthesis of Ag<sub>2</sub>S Quantum Dots and Experimental Determination of the Exciton Bohr Radius. *J. Phys. Chem. C* **2014**, *118*, 4918–4923.
41. Du, Y.; Xu, B.; Fu, T.; Cai, M.; Li, F.; Zhang, Y.; Wang, Q. Near-Infrared Photoluminescent Ag<sub>2</sub>S Quantum Dots from a Single Source Precursor. *J. Am. Chem. Soc.* **2010**, *132*, 1470–1471.